SCIENCE CHINA
Chemistry

• MINI REVIEWS •
· SPECIAL TOPIC · Electrochemical Power Sources

December 2017 Vol.60 No.12: 1483–1493
10.1007/s11426-017-9120-4

High-capacity lithium-rich cathode oxides with multivalent cationic and anionic redox reactions for lithium ion batteries

Enyue Zhao, Xiqian Yu*, Fangwei Wang & Hong Li

Beijing National Laboratory for Condensed Matter Physics, Institute of Physics, Chinese Academy of Sciences, Beijing 100190, China

Received June 15, 2017; accepted August 9, 2017; published online October 20, 2017

Lithium-rich cathode oxides with capability to realize multivalent cationic and anionic redox reactions have attracted much attention as promising candidate electrode materials for high energy density lithium ion batteries because of their ultrahigh specific capacity. However, redox reaction mechanisms, especially for the anionic redox reaction of these materials, are still not very clear. Meanwhile, several pivotal challenges associated with the redox reactions mechanisms, such as structural instability and limited cycle life, hinder the practical applications of these high-capacity lithium-rich cathode oxides. Herein, we review the lithium-rich oxides with various crystal structures. The multivalent cationic/anionic redox reaction mechanisms of several representative high capacity lithium-rich cathode oxides are discussed, attempting to understand the origins of the high lithium storage capacities of these materials. In addition, we provide perspectives for the further development of these lithium-rich cathode oxides based on multivalent cationic and anionic redox reactions, focusing on addressing the fundamental problems and promoting their practical applications.

lithium ion batteries, high capacity, lithium-rich cathode oxides, multivalent cationic redox reaction, anionic redox reaction

Citation: Zhao E, Yu X, Wang F, Li H. High-capacity lithium-rich cathode oxides with multivalent cationic and anionic redox reactions for lithium ion batteries. *Sci China Chem*, 2017, 60: 1483–1493, doi: 10.1007/s11426-017-9120-4

1 Introduction

Rechargeable lithium-ion batteries (LIBs) have occupied a dominant position in the electronics field, and are considered as the most potential energy storage devices to power electric vehicles as well as the electricity grid [1–5]. Large-scale applications of lithium-ion batteries require the increase of the energy density to a higher level. The currently cathode materials for commercialized LIBs mainly include layered structures ($LiCoO_2$, $LiNi_{1/3}Co_{1/3}Mn_{1/3}$) [6–8], olivine $LiFePO_4$ [9,10] and spinel $LiMn_2O_4$ [11,12]. Unfortunately, the specific capacity of these materials is intrinsically limited due to the exchange of at most one Li atom per transition metal during the electrochemical process. Thus, developing lithium-rich (or lithium-excess) cathode materials is a promising option to further increase the theoretical capacity and realize high energy density LIBs [13–17].

Multivalent cationic (transition-metal) ions or multi-electron redox couples (e.g., Cr^{3+}/Cr^{6+}) are necessary to cycle more than one Li atoms in the lithium-rich cathode oxides, while not taking the anionic redox reaction (redox activities on oxygen anions) into account [18–21]. The theoretical capacity of latent lithium-rich cathode oxides with multi-electron cationic redox reaction is shown in Figure 1 (blue column). Besides the multi-electron redox reaction of transition-metal ions, also, the anionic redox reaction can take place in some lithium-rich cathode oxides, which plays a critical role

*Corresponding author (email: xyu@iphy.ac.cn)

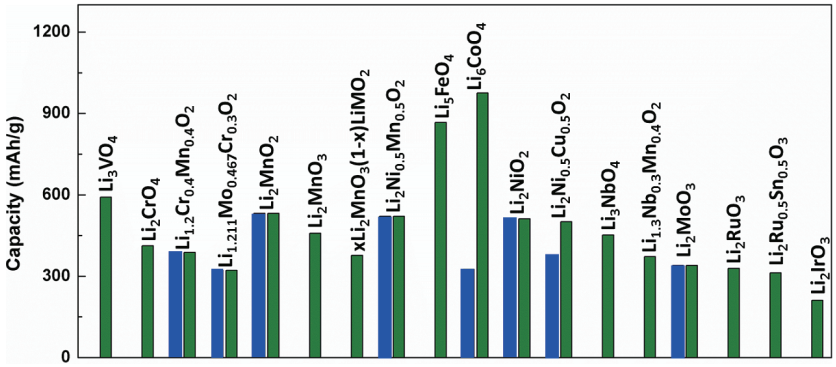

Figure 1 Theoretical capacity of latent lithium-rich cathode oxides with multi-electron cationic redox reaction (blue column) and anionic redox reaction assuming that all Li atoms in oxides can cycle (olive column) (color online).

in achieving higher capacity [22–26]. Figure 1 (olive column) shows the theoretical capacity of latent lithium-rich cathode oxides with anionic redox reaction assuming that all Li atoms in oxides can cycle. These high capacity Li-rich cathode oxides seem to be promising candidate materials for high energy density Li-ion batteries.

In this review, we will focus on several representative high capacity lithium-rich cathode oxides, and present a thorough and fine-grained overview of multivalent cationic and/or anionic redox reaction on them. The pristine crystal structure, electrochemical characteristic and multivalent cationic/anionic redox mechanisms of these materials will be discussed. Finally, promising perspectives for further development of high capacity lithium-rich cathode oxides with multivalent cationic and/or anionic redox reaction will be suggested. We hope that this review will provide valuable insights for designing high capacity lithium-rich cathode oxides for lithium ion batteries.

2 Pristine crystal structures

It can be seen in Figure 1 (blue column) that the theoretical capacity of Li-rich cathode oxides with multi-electron cationic redox couple is much higher than that of the conventional cathode materials. The ultrahigh specific capacity of these materials is associated with multi-electron transfer oxidation/reduction of the transition-metal ions. Among 3d-transtion metals reported so far, anomalous behavior of chromium ions in the host structures has been found from a series of studies on the chromium-based materials [20,27,28]. Trivalent Cr^{3+} in $LiCrO_2$ cannot be reversibly oxidized to Cr^{4+} in lithium batteries [29]. Cr^{3+}, however, is reversibly oxidized to Cr^{6+} when the trivalent Cr ion is substituted for Li/Mn in Li_2MnO_3 [30]. $Li_{1.2}Cr_{0.4}Mn_{0.4}O_2$, as a representative material of solid-solution between $Li[Li_{1/3}Mn_{2/3}]O_2$ and $LiCrO_2$, possess high reversible capacity based on Cr^{3+}/Cr^{6+} three electrons redox reaction [20,27,28]. Figure 2(a) shows the typical refined X-ray diffraction (XRD) patterns of $Li_{1.2}Cr_{0.4}Mn_{0.4}O_2$. It can be seen that all peaks are assigned to a rhombohedral lattice with space group *R*-3*m* except broad peaks found in a 2θ range of 20°–25°, which originate from Li and Mn ordering in transition metal layers [20]. The aberration-corrected high-angle-annular-dark-field (HAADF) and annular-bright-field (ABF) images of pristine $Li_{1.2}Cr_{0.4}Mn_{0.4}O_2$ along the [100] zone axis (based on *C*2/*m* space group) are shown in Figure 2(b, c), in which the distribution of atoms can be clearly seen [20]. The $Li_2Ni_{0.5}Mn_{0.5}O_2$ structure belongs to hexagonal symmetry, in which oxygen ions are arranged in a hexagonally close-packed (hcp) array, Ni and Mn ions are located in all the octahedral sites of one layer and the Li ions are located in all the tetrahedral sites of adjacent layers [19]. The $Li_2Ni_{0.5}Mn_{0.5}O_2$ is very sensitive to air or moisture, and experimental results have shown delithiated phases ($Li_{2-x}Ni_{0.5}Mn_{0.5}O_2$) will easily form when expose it to air [19]. Orthorhombic Li_2NiO_2 with the *Immm* space group, can hold two Li per formula unit with Ni^{2+} and exhibits a higher potential for the Ni^{2+}/Ni^{4+} redox couple compared to that in the layered form of Li_2NiO_2, which is derived from overlithiating $LiNiO_2$ [18]. Figure 2(d) shows the structure of orthorhombic Li_2NiO_2 [31]. $Li_2Cu_{0.5}Ni_{0.5}O_2$, a solid solution of orthorhombic Li_2NiO_2 and Li_2CuO_2, has a very high theoretical capacity based on the Cu^{2+}/Cu^{3+} and Ni^{2+}/Ni^{4+} multi-electron redox couples [31–33]. Due to the similar ionic sizes of Cu^{2+} (0.73 Å) and Ni^{2+} (0.69 Å), $Li_2Cu_{1-x}Ni_xO_2$ can form an orthorhombic structure solid solution over the entire composition range from x=0 to x=1 [32]. It has been reported that structural evolution in $Li_2Cu_{0.5}Ni_{0.5}O_2$ closely likes those of the parent Li_2NiO_2 composition during delithiation process [32].

Antifluorite-type structure Li_6CoO_4 and Li_6MnO_4 have been investigated as cathode materials for lithium ion battery [21,34,35]. Based on the Co^{2+}/Co^{4+} and Mn^{2+}/Mn^{4+} multi-electron redox couples, these materials have high theory capacity. However, it has been reported that 1Li could be extracted from Li_6CoO_4 whereas Li_6MnO_4 could not be delithiated [21]. Figure 2(e) shows the antifluorite-type structure of Li_6CoO_4 with the Li ions represented either as atoms or as LiO_4 tetrahedra [35]. The two lithium ions' local

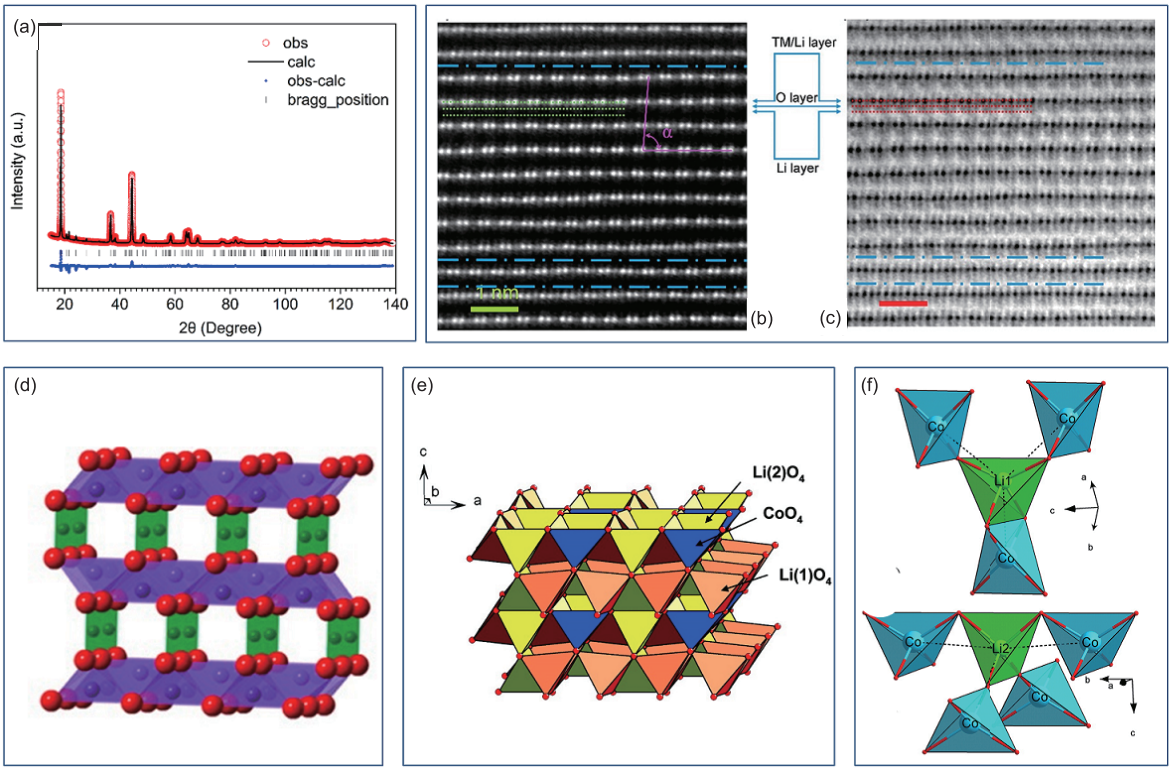

Figure 2 (a) Refined XRD patterns for the pristine $Li_{1.2}Cr_{0.4}Mn_{0.4}O_2$. Atomic resolution (b) HAADF and (c) ABF images for the pristine $Li_{1.2}Cr_{0.4}Mn_{0.4}O_2$ sample along the [100] zone axis. Reprinted with permission of Ref. [20], copyright 2015 American Chemical Society. (d) The schematic structure of orthorhombic Li_2NiO_2. Reprinted with permission of Ref. [31], copyright 2015 American Chemical Society. (e) Structure of Li_6CoO_4 with the Li ions represented as LiO_4 tetrahedra. Reprinted with permission of Ref. [35], copyright 2010 American Chemical Society. (f) Environment for the two Li sites of Li_6CoO_4 showing the local geometry: (top) Li(1) and (bottom) Li(2). Reprinted with permission Ref. [36], copyright 2012 American Chemical Society (color online).

environments in Li_6CoO_4 can be clearly seen in Figure 2(f). The $Li(1)O_4$ tetrahedron shares one edge and two corners with CoO_4 tetrahedra, while the $Li(2)O_4$ tetrahedron shares only its four corners with four CoO_4 tetrahedra [36].

Lithium-rich layered oxides (nominal composition of Li_2MO_3 or $Li[Li_{1/3}M_{2/3}]O_2$, M=Mn, Ru, Ir, etc.) with cation-ordered rocksalt-type structure have been extensively reported as promising high capacity electrode materials for LIBs [23,37–41]. These lithium-rich layered oxides possess a similar structure as that of α-$NaFeO_2$ typed $LiCoO_2$, a commercialized layered cathode material for Li-ion batteries, with the replacement of a portion of transition metal ions by lithium ions in the transition metal layers [42,43]. Figure 3(a) shows the structure of pristine $Li[Li_{1/3}M_{2/3}]O_2$ in the [110] projection, which displays the cubic close-packed O3 stacking of the Li layers and the $Li_{1/3}M_{2/3}O_2$ slabs, where each Li atom is surrounded by six M atoms to form a honeycomb-like ordering pattern [22]. Li_2MnO_3 is almost electrochemically inert because of its intrinsic insulativity and unachievable oxidation of Mn^{4+} during delithiation process. Meanwhile, all the octahedral sites of the rocksalt structure in the Li_2MnO_3 are fully occupied, which make the similarly insertion of Li into Li_2MnO_3 is not feasible [44,45]. However, the fact is that Li_2MnO_3 is electrochemically active, presumably due to the contribution of anionic for redox reaction. Due to the similar structure between $Li[Li_{1/3}Mn_{2/3}]O_2$ and $LiCoO_2$, further attempts to improve the electrochemical properties resulted in the discovery of a new series of composite cathode materials such as $xLi_2MnO_3\cdot(1-x)LiMeO_2$ (Me=Ni, Co, Fe, etc.) which exhibit higher capacity and excellent stability [46–49]. Nevertheless, these integrated materials present complex layered structures as there is still ambiguity whether the pristine structure of them consists of two phases or a single phase. Figure 3(b) shows the typical XRD patterns of lithium-rich $xLi_2MnO_3\cdot(1-x)LiMeO_2$ materials, the superstructure peaks between 20° and 25° is associated with the ordering of cations (Li, Me and Mn) in the transition metal layer of the layered lattice [50]. Li_2RuO_3 has a minor structural difference compared with Li_2MnO_3. *C*2/*c* space group is usually used to describe Li_2RuO_3 while *C*2/*m* space group is used to describe Li_2MnO_3 [41,51]. The difference can be ascribed to a distortion of the rocksalt oxygen stacking. Also, Miura *et al*. [52] suggested Li_2RuO_3 can be better described in the $P2_1/m$ space group due to the formation of Ru-Ru dimers. Different from Li_2MnO_3, deinsertion and reinsertion of Li^+ in Li_2RuO_3 is possible, because of the Ru^{4+}/Ru^{5+} redox couple. Li_2RuO_3 can also form a series of solid solution, including $Li_2Ru_{1-y}Mn_yO_3$, $Li_2Ru_{1-y}Sn_yO_3$ and $Li_2Ru_{1-y}Ti_yO_3$,

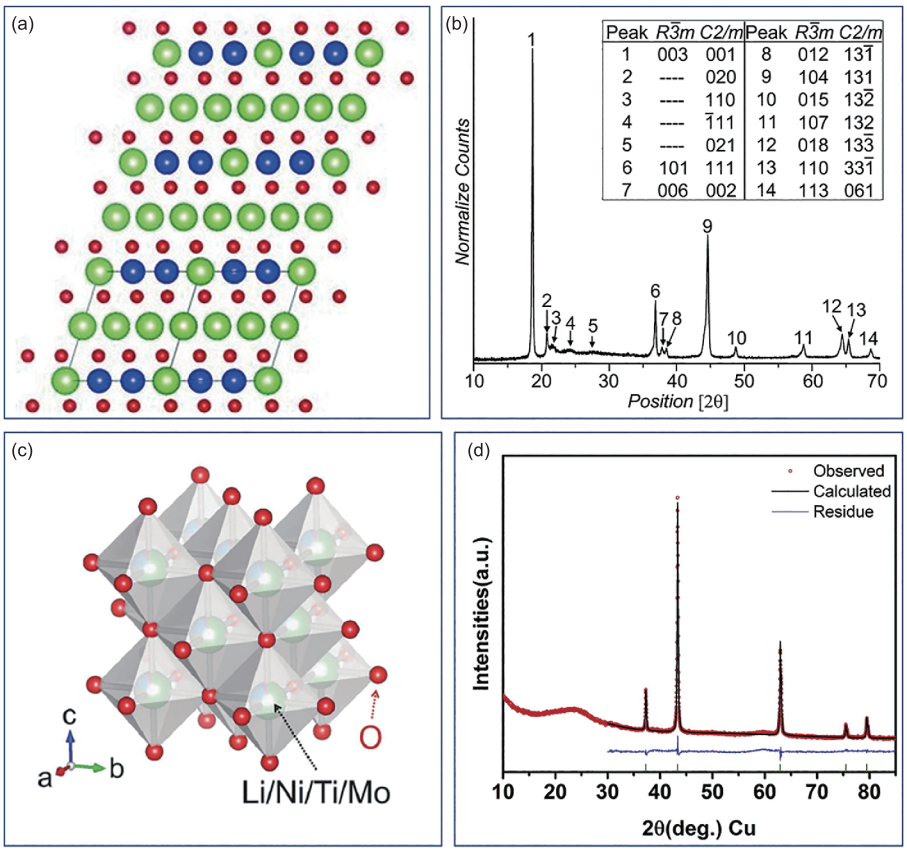

Figure 3 (a) Structure of pristine $Li[Li_{1/3}M_{2/3}]O_2$ in the [110] projection. Throughout the figures: M is blue, Li is green, and O is red. Modified from reference [22], and reprinted with permission of Ref. [22], copyright 2015 American Association for the Advancement of Science. (b) XRD pattern of lithium-rich layered $xLi_2MnO_3\cdot(1-x)LiMeO_2$ materials with major peaks numbered. The peaks are labeled according to *R*-3*m* and *C*2/*m* symmetry in the inset table. The dashes for peaks 2–5 in the *R*-3*m* column indicate that there are no allowed reflections at these positions for the *R*-3*m* space group. Reprinted with permission of Ref. [50], copyright 2011 American Chemical Society. (c) Schematic diagram of disordered rocksalt-type solid-solution compounds between $LiNi_{0.5}Ti_{0.5}O_2$ and $Li_{1.6}Mo_{0.4}O_2$. Reprinted with permission of Ref. [56], copyright 2015 Royal Society of Chemistry. (d) Refined XRD patterns of the cation-disordered rocksalt structure oxides. Reprinted with permission of Ref. [59], copyright 2015 Elsevier.

with Li_2MnO_3, Li_2SnO_3 and Li_2TiO_3 [41,51,53,54].

It has been reported the anionic redox reaction contributes capacity for lithium-rich cathode oxides with cation-disordered rocksalt structure [55–58]. Figure 3(c) shows a typical schematic diagram of disordered rocksalt-type solid-solution compounds between $LiNi_{0.5}Ti_{0.5}O_2$ and $Li_{1.6}Mo_{0.4}O_2$ [56]. Figure 3(d) shows the typical XRD patterns of the cation-disordered rocksalt structure oxides, which belong to the space group of *Fm*-3*m* [59]. In this cation-disordered rocksalt structure, lithium ions and transition metal ions homogeneously distributed in the atomic site 4a, while anionic ions distributed in the site 4b [59]. Generally, the well-crystallized cation-disordered rocksalt samples are considered to be electrochemically inactive. Recently, Lee *et al*. [55] reported the formation of a percolating network for lithium diffusion in the lithium-rich cation-disordered $Li_{1.211}Mo_{0.467}Cr_{0.3}O_2$ material, also, their calculation results according density functional theory showed facile macroscopic lithium diffusion in the lithium-percolating network is energetically possible in the lithium-excess cation-disordered rocksalt-type structure. Yabuuchi *et al*. [57] reported high capacity Li_3NbO_4-based system electrode materials with cation-disordered rocksalt structure. Li_3NbO_4 crystal structure is composed of four edge-shared NbO_6-octahedras (Nb_4O_{16} tetramer), and Li ions are accommodated in a body-centered cubic lattice of the Nb_4O_{16} tetramers. $Li_{1.3}Nb_{0.3}Mn_{0.4}O_2$, as a solid solution of Li_3NbO_4 and $LiMnO_2$, possesses the enriched Li amount, and in which Li ions migration throughout the particle by site percolation is feasible [57]. Li_2VO_3, an electrochemical reduction product of $LiVO_3$ in lithium batteries, has also been reported to be electrochemically active as a lithium-rich cation-disordered rocksalt phase [60].

3 High-capacity and multivalent cationic/anionic redox mechanisms

Multi-electron cationic redox reaction can provide a way to overcome the capacity limitation caused by the usual limit of one electron per transition metal in an acceptable voltage range that applies to cations in most of cathode materials. As mentioned above, $Li_{1.2}Cr_{0.4}Mn_{0.4}O_2$ possess high theoretical capacity of 387 mA h/g based on multi-electron transfer

of Cr^{3+}/Cr^{6+}. In addition, it has been proved experimentally that the reversible Cr^{3+}/Cr^{6+} multi-electron redox reaction in $Li_{1.2}Cr_{0.4}Mn_{0.4}O_2$ can only be achieved in a wide voltage range 1.0–4.8 V [20]. During the charge and discharge processes, there is a reversible migration of the Cr ions between octahedral and tetrahedral sites, which results in a large extent of cations mixing between transition metal and lithium layers. Lyu *et al*. [20] using aberration-corrected high-angle-annular-dark-field (HAADF) and annular-bright-field (ABF) scanning transmission electron microscopy (STEM) techniques disclosed the structural evolution of $Li_{1.2}Cr_{0.4}Mn_{0.4}O_2$ during the first charge and discharge processes. The structural evolution schematic is shown in Figure 4.

Similar to Cr^{3+}/Cr^{6+} redox couple in $Li_{1.2}Cr_{0.4}Mn_{0.4}O_2$, Ni^{2+}/Ni^{4+} redox couple also has the potential to realize multi-electron transfer in the Li_2NiO_2 system materials. The research of the electrochemical properties and phase stability of the orthorhombic *Immm* structure Li_2NiO_2 was conducted by Kang *et al*. [18]. Their experimental results and first principles calculations all indicate that the orthorhombic *Immm* structure is rather prone to phase transformation to a close-packed layered structure during the charge and discharge process. A conclusion that crystal field effects may not be large enough to stabilize Ni^{2+} in a square planar environment was obtained by detailed analyzing the crystal field energy difference between octahedral and square-planar coordinated Ni^{2+}. Lithium-rich cathode oxides $Li_2Cu_{0.5}Ni_{0.5}O_2$, which also possesses potential Ni^{2+}/Ni^{4+} redox couple with multi-electron transfer, have a very high theoretical capacity, and the capacity is nearly 400 mA h/g during the first delithiation, however, only ~125 mA h/g is reversible [31,32]. The irreversible capacity during the first cycle can be attributed to the oxygen evolution and structural transformations. Oxygen evolves before the $Cu^{2+/3+}$ or $Ni^{3+/4+}$ transitions are obtained. Ruther *et al*. [31] found that $Li_2Cu_{0.5}Ni_{0.5}O_2$ loses long-range order during charge and, similar to Li_2NiO_2, the phase transformation from orthorhombic to a partially layered structure also occurred. A complete understanding of the chemical and structural changes occurred on lithium-rich cathode oxides with multi-electron redox during the electrochemical reaction process is very important for taking the full advantage of the multi-electron redox processes.

Numerous research studies have shown that, the high capacity of some Li-rich cathode oxides is associated with the anionic redox reaction. The capacity of Li- and Mn-rich layered cathode materials, for instance, depends not solely on the cationic redox reactions, but also the anionic redox reaction [40,61,62]. The future realization of reversible anionic redox reaction may offer a great opportunity for the development of high energy density Li-ion batteries. It can be clearly seen in the Figure 1(b) that, all the lithium-rich cathode oxides show ultrahigh theory specific capacity assuming all the Li ions in the oxides can be reversibly intercalated/deintercalated. Obviously, anionic ions must participate in the charge compen-

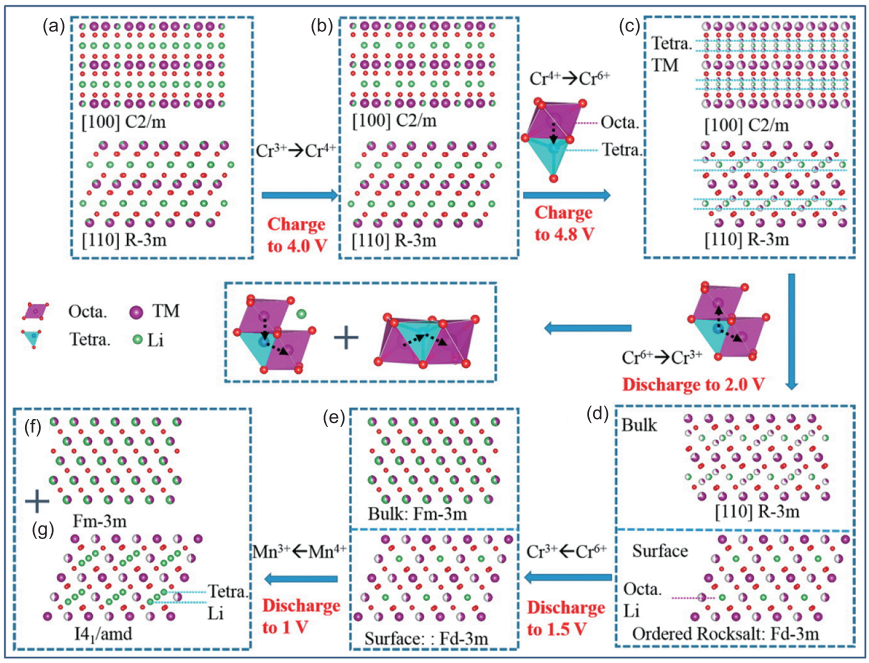

Figure 4 The structure models of the (a) pristine states and different charge states (b, c). (b) and (c) are built both in the *C*2/*m* space group and *R*-3*m* space group to describe that the lithium ions in the 2c sites delithiated first. The [010] direction in *C*2/*m* is similar to [110] in the *R*-3*m* space group. During the discharge state of (d) 2 V and (e) 1.5 V, the surface and the subsurface structures are built, respectively. The 1 V state contains both (f) rocksalt and (g) $I4_1$ structures. Also, the migration of transition metal ions is shown. Reprinted with permission of Ref. [20], copyright 2015 American Chemical Society (color online).

sation in the electrochemical reaction to realize the ultrahigh theory capacity. Numerous literature reports have confirmed the origin of the high reversible capacity in lithium-rich cathode oxides is closely associated with the anionic ion redox reaction [22,63,64]. However, how anionic ions involve into the charge compensation, and how the oxides structure responds to such anionic activities are still under fierce debate.

As to the traditional layered cathode oxides, including $LiCoO_2$, $LiNi_{0.5}Mn_{0.5}O_2$, $LiNi_{1/3}Co_{1/3}Mn_{1/3}O_2$, etc, the redox reactions involved in the Li intercalation/deintercalation mechanism are associated with Co^{3+}/Co^{4+} and/or Ni^{2+}/Ni^{4+}, whereas the oxidation of Mn^{4+} does not occurred [65,66]. The reversible capacity of these cathode materials is limited within 200 mA h/g. However, the reversible capacity of Li- and Mn-rich cathode oxides, such as $Li_{1.2}Mn_{0.54}Ni_{0.13}Co_{0.13}O_2$, can be higher than 300 mA h/g in the voltage range of 2.0–4.8 V [14,44]. Such high capacity far exceeds the expected one, which is calculated based on the redox reaction of transition metal cations (Co^{3+}/Co^{4+} and Ni^{2+}/Ni^{4+}). Lots of research works have concentrated on the understanding of this abnormal capacity, and the general viewpoint is that this extra capacity is originated from the reversible oxygen redox couple. Early reports by Lu *et al*. [67,68] suggested that the loss of oxygen from crystal lattice upon a high degree of delithiation led to the high capacity. Koga *et al*. [69] reported that a mixture of two phases is formed in the high voltage plateau, and the origin of which is due to the difference in stability for oxidized oxygen ions between the surface and the bulk of the lithium-rich $Li_{1.2}Mn_{0.54}Ni_{0.13}Co_{0.13}O_2$ oxides. Meanwhile, they proposed the mechanism that the reversible oxygen oxidation occurs within the bulk without oxygen loss and the irreversible oxygen loss occurred at the surface with densification of the host structure [70]. Armstrong *et al*. [71] using the differential electrochemical mass spectrometry technique directly observed the oxygen gas evolution in lithium-rich cathode oxides during the first charge process. Also, they demonstrated the formation of localized oxygen hole without O–O dimerization which they believed to be accounted for the extra reversible capacity in lithium-rich $Li_{1.2}Mn_{0.54}Ni_{0.13}Co_{0.13}O_2$ [63]. Wang *et al*. took the lithium-rich $Li_{1.2}Mn_{0.54}Ni_{0.13}Co_{0.13}O_2$ ($Li_2MnO_3{\cdot}LiNi_{1/3}Co_{1/3}Mn_{1/3}O_2$) oxides as an example, and detailed studied its electrochemical working mechanisms which can be clearly shown in Figure 5(a–d) [15]. Figure 5(a, b) shows the typical first charge/discharge voltage curves and the corresponding dQ/dV plots of $Li_{1.2}Mn_{0.54}Ni_{0.13}Co_{0.13}O_2$ at 0.1 and 2.0 C (1 C=250 mA h/g) rates. Process (I) and Process (II) in Figure 5(c, d) represent the delithiation of $LiNi_{1/3}Co_{1/3}Mn_{1/3}$ and Li_2MnO_3, respectively. Process (III) and Process (IV) in Figure 5(c) show the discharge process taking no account of reversible oxygen species, they found the high discharge capacity of Li-rich oxides cannot be fully accounted assuming only the formation of irreversible oxygen species. They suggested the charge/discharge mechanism with reversible oxygen redox couple can be assigned into five processes as shown in Figure 5(d). In short, the Process (II) in Figure 5(d) is irreversible which is correlated with Process (V). The high capacity of Li-rich cathode oxides should be ascribed to the Processes (III), (IV) and (V). The oxygen activating reactions on the cathode's surface during electrochemical cycling have very important effects on the structural stability and electrochemical performances of Li-rich cathode oxides. Hy *et al*. [72] observed the oxygen-related surface reactions using the *in situ* surfaced-enhanced Raman spectroscopy technique, and they confirm the formation of Li_2O during the extended plateau. The proposed surface reaction mechanism of Li-rich cathode oxides oxygen activating members is shown in Figure 5(e) [72].

In recent years, many studies aiming at revealing the new anionic ions redox reaction mechanism of Li-rich cathode oxides containing 4d and 5d metals (Ru, Ir, etc.) have been carried out [23,54]. Tarascon *et al*. [41] demonstrated the oxygen redox process is an integral part of the mechanism accounting for the high capacity displayed by Li-rich cathode oxides through the studies of $Li_2Ru_{1-y}Mn_yO_3$. Later, they studied the $Li_2Ru_{1-y}Sn_yO_3$ series, in which Sn^{4+} ($4d^{10}$) is not easily reducible into Sn^{2+} and suggested the reactivity of Li-rich cathode oxides towards Li entails cumulative cationic and anionic reversible redox processes, owing to the d-sp hybridization associated with a reductive coupling mechanism [51]. The reductive coupling mechanism that they proposed, as well as calculations accounting for superoxo-like species and experimental results of detected oxygen release are shown in Figure 6(a–d) [51]. Furthermore, they used Li_2IrO_3 as a model compound, in which Ir is a 5d metal and can increase the covalency and minimize the unwanted cationic migration, to visualize the O–O dimers via transmission electron microscopy and neutron diffraction [22]. Figure 6(e–h) shows the TEM results of the charged $Li_{0.5}IrO_3$ sample, the O–O pairs with short projected distances are marked with dumbbells in Figure 6(g) [22]. Their findings deepen the understanding of peroxo formation and localization, O_2 recombination, which are closely related to the reversibility of the anionic redox reactions.

Ceder *et al*. [73] identified the structural and chemical origin of the oxygen redox activity in layered and cation-disordered Li-rich cathode oxides using ab initio calculations. They suggested oxygen oxidation in Li-rich oxides mainly occurs by extracting labile electrons from unhybridized O 2p states sitting in Li–O–Li configurations and, thus is unrelated to any hybridized TM–O states. The structural and chemical origin of the preferred oxygen oxidation along the Li–O–Li configuration is shown in Figure 7(a–d) [73]. Experimentally, the high capacity of several cation-disordered Li-rich cathode oxides ($Li_{1.21}Mo_{0.467}Cr_{0.3}O_2$, $Li_{2+2x}Mn_{1-x}Ti_{1-x}O_4$, $Li_{1.2}Ni_{1/3}Ti_{1/3}$-

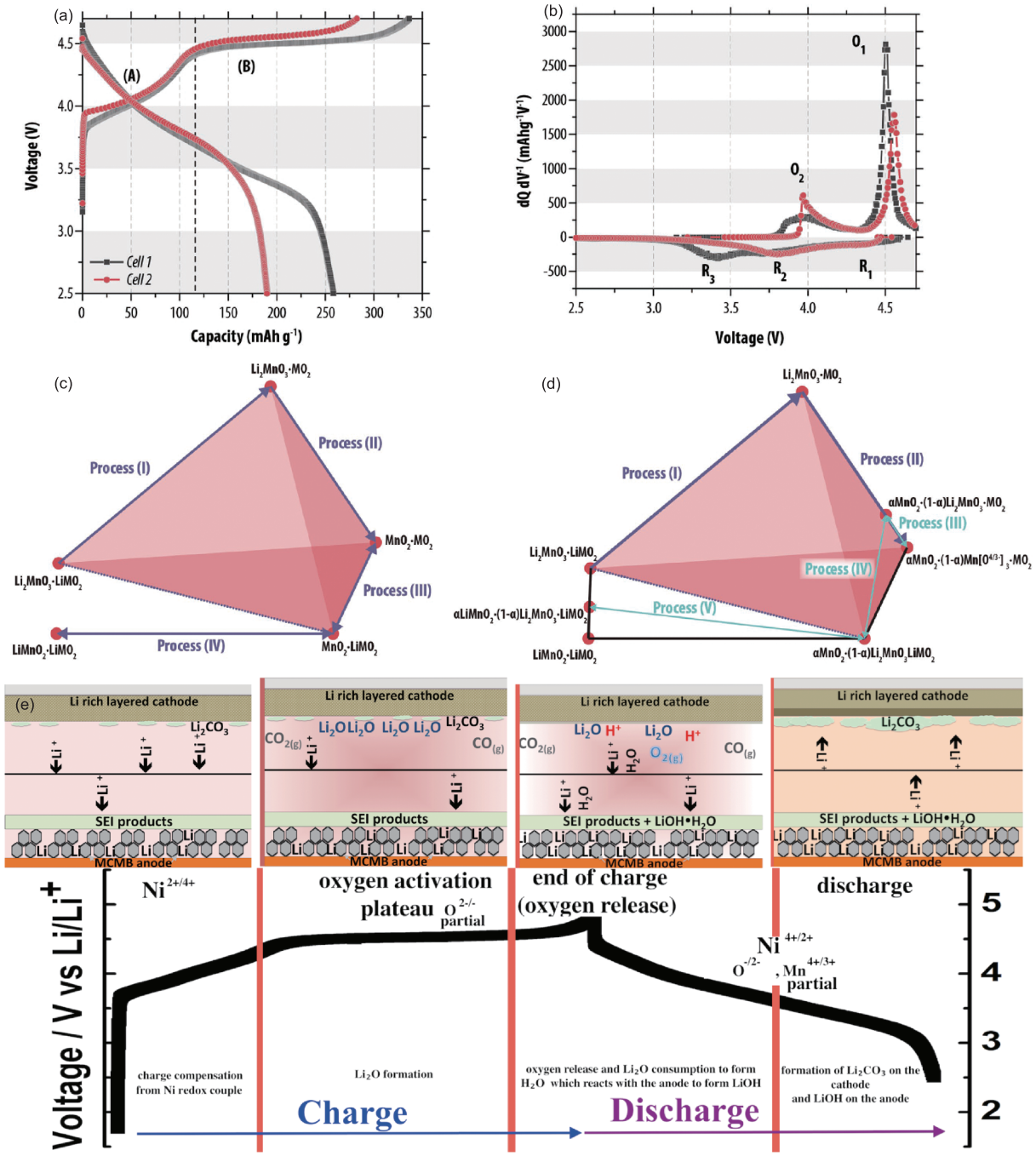

Figure 5 (a) First charge/discharge voltage curves and (b) the corresponding dQ/dV plots of $Li_{1.2}Mn_{0.54}Ni_{0.13}Co_{0.13}O_2$ at 0.1 and 2.0 C (1 C=250 mA h/g) rates. (c, d) Compositional phase diagrams showing two different electrochemical reaction pathways for the $Li_2MnO_3{\cdot}LiMO_2$ (M=$Ni_{1/3}Co_{1/3}Mn_{1/3}$) electrode. Reprinted with permission of Ref. [15], copyright 2016 Wiley-VCH. (e) Proposed surface reaction mechanism of $Li[Ni_xLi_{(1-2x)/3}Mn_{(2-x)/3}]O_2$ for oxygen activating members during charging and discharging (top) and charging/discharging curve showing the different process (bottom). Reprinted with permission of Ref. [72], copyright 2014 American Chemical Society (color online).

$Mo_{2/15}O_2$, etc.) has been demonstrated to be originated from both the anionic and transition-metal redox reaction [55–58]. In cation-disordered system $Li_{(4-y)/3}Nb_{1/3}Mn_{1/3}O_2$, Yabuuchi *et al*. [57] clarified the role of anionic ions for the charge compensation by using *ab initio* calculations. The partial densities of states of $Li_{(4-y)/3}Mn_{1/3}Nb_{1/3}O_2$ at different delithiation states were calculated as shown in Figure 7(e), and X-ray absorption spectroscopy (XAS) with both hard and soft X-rays provided the experimental proofs. Although there are many challenges for such oxygen active intercalation Li-rich oxides, all of these theoretical and experimental findings lead to a deep understanding of the anionic redox reaction which is favorable for the development of higher-energy density cathode materials.

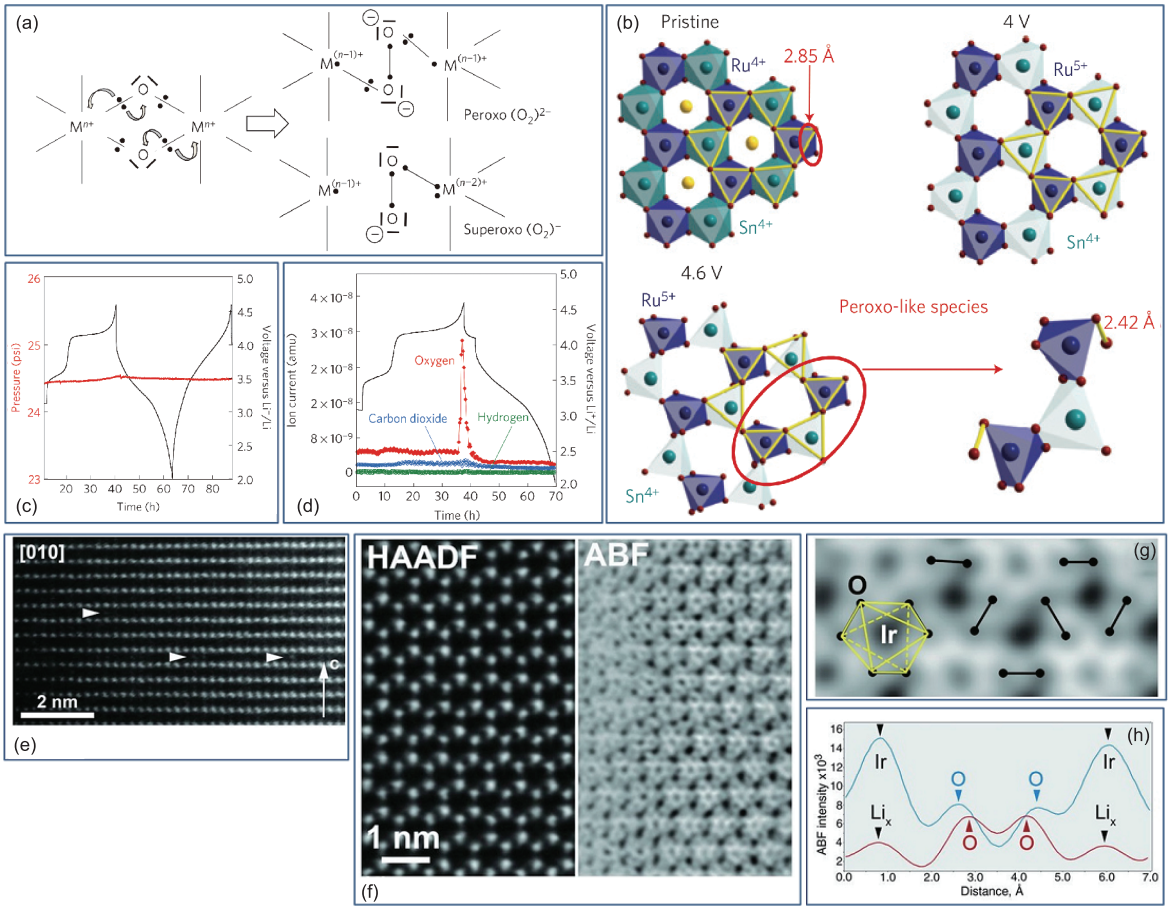

Figure 6 (a) The reductive coupling mechanism of two oxo-ligands coordinated to the transition metals leads to a single or double metal reduction depending on the coordination mode of the O_2 moiety. (b) Representation of one LiM_2 honeycomb layer of the $Li_xRu_{0.5}Sn_{0.5}O_3$ as obtained from DFT calculations after full structural relaxation for the lithium compositions x=2 (pristine), 1.5 (4 V) and 0.75 (4.6 V). The Ru, Sn, O and Li atoms are represented in blue, green, red and yellow, respectively. The yellow bonds are shown to follow the distortion of the oxygen network. (c) Oxygen pressure evolution during the first charge, first discharge and second charge for a $Li_xRu_{0.5}Sn_{0.5}O_3$ cell. (d) Gas profile of the first cycle for the same cell cycled at room temperature. Reprinted with permission of Ref. [51], copyright 2013 Macmillan Publishers Limited. (e) [010] HAADF-STEM image of the charged $Li_{0.5}IrO_3$ sample, demonstrating the ordered sequence of the Ir layers corresponding to the O1-type structure. (f) [001] HAADF-STEM and ABF-STEM images of the same sample. (g) Enlarged ABF-STEM image and (h) ABF intensity profiles along the O–O pairs with long (blue) and short (red) projected distances. Reprinted with permission of Ref. [22], copyright 2015 American Association for the Advancement of Science (color online).

4 Conclusions and perspective

Lithium-rich cathode oxides are attractive candidate cathode materials for the next generation lithium ion batteries due to their large capacities based on the multivalent transition metals redox reaction and potential anionic redox reactions. Compared with conventional cathode materials, including Li-CoO_2, $LiNi_{0.5}Mn_{0.5}O_2$, $LiFePO_4$, $LiMn_2O_4$ etc., lithium-rich cathode oxides with multivalent cationic and anionic redox reactions can cycle >1 Li^+ per transition metal and liberate the number of electrons the transition metal exchanging per unit mass in the electrochemical activities [1,5,48,74,75]. During the past decades, lithium-rich cathode oxides have received wide attention in experimental and theoretical researches. Table 1 briefly summarizes the developed lithium-rich cathode oxides with multivalent cationic and/or anionic redox reactions. It can be seen Li and Mn-rich layered cathode materials show the most potential in practical applications for high energy LIBs, although there are still some problems need to be overcome, such as capacity degradation, voltage fade.

In this brief review, several representative high capacity lithium-rich cathode oxides with multivalent cationic and/or anionic redox reactions were revisited. We generalized the pristine crystal structure of these materials, focused on the relationship between electrochemical characteristics and structure, and reviewed the multivalent cationic and anionic redox reaction mechanisms associated with their high capacity. With regard to the mechanisms of the multivalent cationic and anionic redox reactions, it seems to be complex and debatable. Taking $Li_2Ni_{0.5}Cu_{0.5}O_2$ as an example, the capacity of this material should, theoretically, depend on the multi-electron Ni^{2+}/Ni^{4+} and Cu^{2+}/Cu^{3+} redox couple. However, experiments results show that a reversible $Ni^{2+/3+}$ couple and oxy-

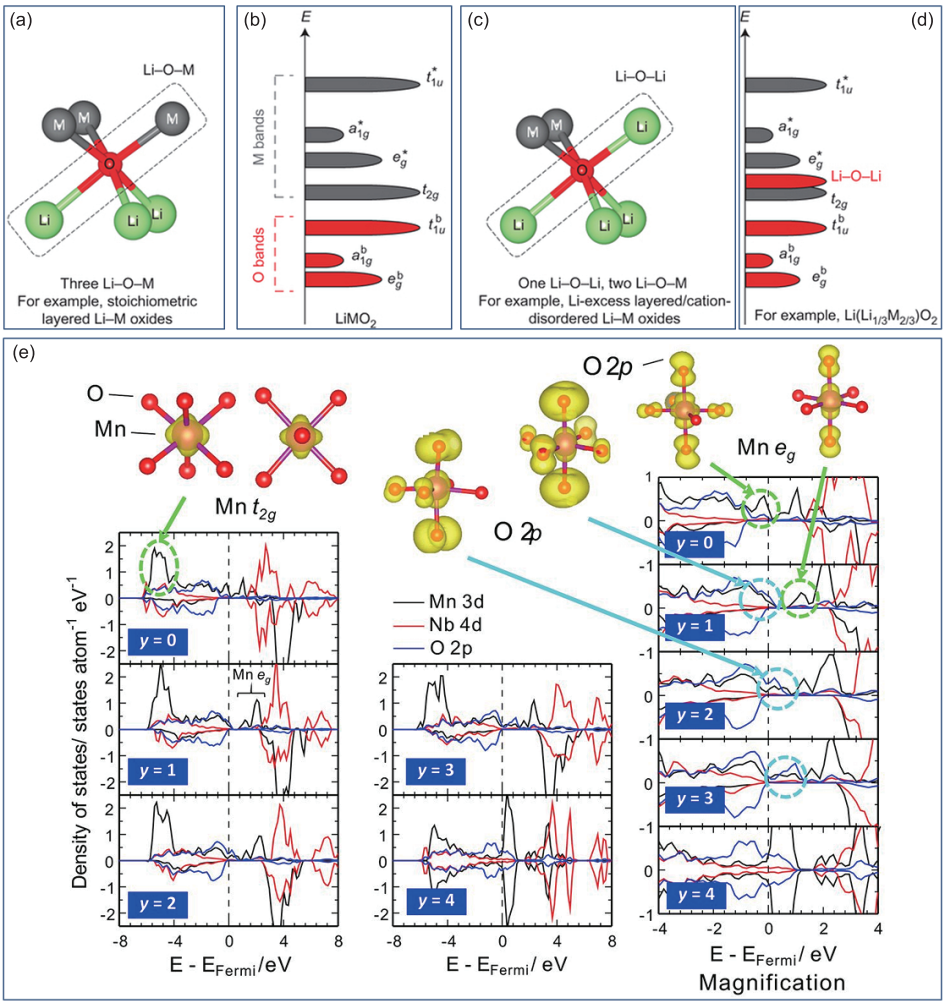

Figure 7 (a) Local atomic coordination around oxygen consisting of three Li–O–M configurations in stoichiometric layered Li metal oxides (Li–M oxides). (b) Chematic of the band structure for stoichiometric layered Li–M oxides such as $LiCoO_2$. (c) Local atomic coordination around oxygen with one Li–O–Li and two Li–O–M configurations in Li-excess layered or cation-disordered Li–M oxides. (d) Schematic of the band structure for Li-excess layered Li–M oxides such as Li_2MnO_3. Reprinted with permission of Ref. [73], copyright 2016 Macmillan Publishers Limited. (e) Partial densities of states with electrochemical charging in $Li_{(4-y)/3}Mn_{1/3}Nb_{1/3}O_2$ as calculated with the DFT method. Reprinted with permission of Ref. [57], copyright 2015 National Academy of Sciences (color online).

Table 1 The electrochemical performances of Li-rich cathode oxides with multivalent cationic and/or anionic redox reactions

Lithium-rich cathode oxides	Initial specific capacity (mA h/g)	Measurement conditions	Ref.
$Li_{1.2}Cr_{0.4}Mn_{0.4}O_2$	~162	2.0–4.8 V, 38.7 mA/g, RT	[20]
$Li_{1.2}Mn_{0.54}Ni_{0.13}Co_{0.13}O_2$	~260	2.5–4.7 V, 25 mA/g, RT	[15]
Li_2NiO_2	~240	1.5–4.6 V, 12.5 mA/g, RT	[18]
$Li_2Cu_{0.5}Ni_{0.5}O_2$	~320	1.5–4.3 V, 70 mA/g, RT	[31]
$Li_{1.3}Nb_{0.3}Mn_{0.4}O_2$	~280	1.5–4.8 V, 10 mA/g, 60 °C	[57]
$Li_2Ru_{0.75}Sn_{0.25}O_3$	~220	2.0–4.6 V, 15 mA/g, RT	[51]
$Li_2Ir_{0.75}Sn_{0.25}O_3$	~158	2.5–4.6 V, 10 mA/g, RT	[22]

gen redox reaction contribute to the capacity, and almost no evidence for the formation of Cu^{3+} [31,32]. Multi-electron transfer cationic redox reaction and anionic redox reaction may simultaneously participate in the charge compensation over the electrochemical process. For anionic redox reaction, a reversible oxo- (O^{2-}) transforms to peroxo-like $(O_2)^{n-}$ (n=1, 2, 3) during the electrochemical reaction may be a generally accepted mechanism, in particular for lithium rich compounds containing transition metal cations with strong covalency [23,51,63].

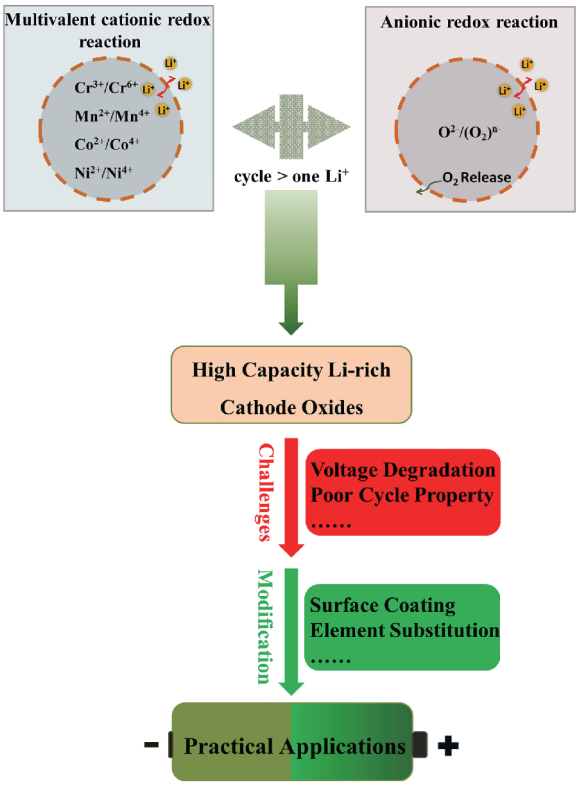

Figure 8 Challenges and further work for the practical applications of Li-rich cathode oxides with multivalent cationic and/or anionic redox reactions (color online).

Despite the tempting prospects of lithium-rich cathode oxides with ultrahigh capacity, there are several challenges restricting their further practical applications. Typically, the irreversible O_2 gas release can lead to a series of negative effects on the electrochemical performances of electrode materials [47,76]. Multifarious challenges for lithium-rich cathode oxides with multivalent cationic and/or anionic redox reactions, and the further work for their practical applications are summarized in Figure 8. The origin of low initial Coulombic efficiency is directly related to the O_2 gas release. Voltage fade during cycling will continuously decrease the energy density of lithium-rich cathode oxides, and seriously restricts their practical applications. Various synthesis strategies, element substitution, and surface modification have been proven to be effective approaches to optimize the electrochemical performance of lithium-rich cathode oxides. For instance, surface modification could stabilize the electrode-electrolyte interface, improve the ionic or electronic conductivity when appropriate surface modification materials are used. They can also suppress irreversible phase transformation, decrease cationic disorder in crystal sites, and reduce sensitivity to acid species (e.g. HF) generated in the electrolyte. Finally, we believe that the clarification of redox reaction mechanisms would provide valuable insights for designing high capacity lithium rich cathode oxides and thus accelerate their practical applications for high energy density lithium ion batteries.

Acknowledgments This work was supported by the National Key Research and Development Program of China (2016YFA202500), the "One Hundred Talent Project" of the Chinese Academy of Sciences, and the National Natural Science Foundation of China (11675255).

Conflict of interest The authors declare no conflict of interest.

1 Cheng F, Liang J, Tao Z, Chen J. *Adv Mater*, 2011, 23: 1695–1715
2 Cheng F, Tao Z, Liang J, Chen J. *Chem Mater*, 2008, 20: 667–681
3 Tarascon JM, Armand M. *Nature*, 2001, 414: 359–367
4 Sun H, Mei L, Liang J, Zhao Z, Lee C, Fei H, Ding M, Lau J, Li M, Wang C, Xu X, Hao G, Papandrea B, Shakir I, Dunn B, Huang Y, Duan X. *Science*, 2017, 356: 599–604
5 Guo YG, Hu JS, Wan LJ. *Adv Mater*, 2008, 20: 2878–2887
6 Zhou P, Meng H, Zhang Z, Chen C, Lu Y, Cao J, Cheng F, Chen J. *J Mater Chem A*, 2017, 5: 2724–2731
7 Jiang KC, Xin S, Lee JS, Kim J, Xiao XL, Guo YG. *Phys Chem Chem Phys*, 2012, 14: 2934–2939
8 Zhao E, Fang L, Chen M, Chen D, Huang Q, Hu Z, Yan Q, Wu M, Xiao X. *J Mater Chem A*, 2017, 5: 1679–1686
9 Wu XL, Jiang LY, Cao FF, Guo YG, Wan LJ. *Adv Mater*, 2009, 21: 2710–2714
10 Su J, Wu XL, Yang CP, Lee JS, Kim J, Guo YG. *J Phys Chem C*, 2012, 116: 5019–5024
11 Xiao J, Chen X, Sushko PV, Sushko ML, Kovarik L, Feng J, Deng Z, Zheng J, Graff GL, Nie Z, Choi D, Liu J, Zhang JG, Whittingham MS. *Adv Mater*, 2012, 24: 2109–2116
12 Manthiram A, Knight JC, Myung ST, Oh SM, Sun YK. *Adv Energ Mater*, 2016, 6: 1501010–1501032
13 Shi JL, Zhang JN, He M, Zhang XD, Yin YX, Li H, Guo YG, Gu L, Wan LJ. *ACS Appl Mater Interfaces*, 2016, 8: 20138–20146
14 Zhang K, Han X, Hu Z, Zhang X, Tao Z, Chen J. *Chem Soc Rev*, 2015, 44: 699–728
15 Wang J, He X, Paillard E, Laszczynski N, Li J, Passerini S. *Adv Energ Mater*, 2016, 6: 1600906–1600922
16 Zhao E, Hu Z, Xie L, Chen X, Xiao X, Liu X. *RSC Adv*, 2015, 5: 31238–31244
17 Zhao E, Liu X, Zhao H, Xiao X, Hu Z. *Chem Commun*, 2015, 51: 9093–9096
18 Kang K, Chen CH, Hwang BJ, Ceder G. *ChemMater*, 2004, 16: 2685–2690
19 Johnson CS, Kim JS, Kropf AJ, Kahaian AJ, Vaughey JT, Fransson LML, Edström K, Thackeray MM. *Chem Mater*, 2003, 15: 2313–2322
20 Lyu Y, Zhao N, Hu E, Xiao R, Yu X, Gu L, Yang XQ, Li H. *Chem Mater*, 2015, 27: 5238–5252
21 Lim YG, Kim D, Lim JM, Kim JS, Yu JS, Kim YJ, Byun D, Cho M, Cho K, Park MS. *J Mater Chem A*, 2015, 3: 12377–12385
22 McCalla E, Abakumov AM, Saubanère M, Foix D, Berg EJ, Rousse G, Doublet ML, Gonbeau D, Novák P, Van Tendeloo G, Dominko R, Tarascon JM. *Science*, 2015, 350: 1516–1521
23 Pearce PE, Perez AJ, Rousse G, Saubanère M, Batuk D, Foix D, McCalla E, Abakumov AM, Van Tendeloo G, Doublet ML, Tarascon JM. *Nat Mater*, 2017, 16: 580–586
24 Li BA, Shao RW, Yan HJ, An L, Zhang B, Wei H, Ma J, Xia DG, Han XD. *Adv Funct Mater*, 2016, 269: 1330–1337
25 Kim S, Cho W, Zhang X, Oshima Y, Choi JW. *Nat Commun*, 2016, 7: 13598–13605
26 Chen H, Islam MS. *Chem Mater*, 2016, 28: 6656–6663
27 Ammundsen B, Paulsen J, Davidson I, Liu RS, Shen CH, Chen JM,

Jang LY, Lee JF. *J Electrochem Soc*, 2002, 149: A431
28 Lu Z, Dahn JR. *J Electrochem Soc*, 2002, 149: A1454
29 Sivakumar V, Ross CA, Yabuuchi N, Shao-Horn Y, Persson K, Ceder G. *J Electrochem Soc*, 2008, 155: P83
30 Yabuuchi N, Yamamoto K, Yoshii K, Nakai I, Nishizawa T, Omaru A, Toyooka T, Komaba S. *J ElectroChem Soc*, 2013, 160: A39–A45
31 Ruther RE, Zhou H, Dhital C, Saravanan K, Kercher AK, Chen G, Huq A, Delnick FM, Nanda J. *Chem Mater*, 2015, 27: 6746–6754
32 Ruther RE, Samuthira Pandian A, Yan P, Weker JN, Wang C, Nanda J. *Chem Mater*, 2017, 29: 2997–3005
33 Xu J, Renfrew S, Marcus MA, Sun M, McCloskey BD, Tong W. *J Phys Chem C*, 2017, 121: 11100–11107
34 Noh M, Cho J. *J ElectroChem Soc*, 2012, 159: A1329–A1334
35 Carlier D, Ménétrier M, Delmas C. *J Phys Chem C*, 2010, 114: 4749–4755
36 Zhang Y, Castets A, Carlier D, Ménétrier M, Boucher F. *J Phys Chem C*, 2012, 116: 17393–17402
37 Qing RP, Shi JL, Xiao DD, Zhang XD, Yin YX, Zhai YB, Gu L, Guo YG. *Adv Energ Mater*, 2016, 6: 1501914–1501919
38 Jiang KC, Wu XL, Yin YX, Lee JS, Kim J, Guo YG. *ACS Appl Mater Interfaces*, 2012, 4: 4858–4863
39 Hu M, Pang X, Zhou Z. *J Power Sources*, 2013, 237: 229–242
40 Zhang S, Gu H, Pan H, Yang S, Du W, Li X, Gao M, Liu Y, Zhu M, Ouyang L, Jian D, Pan F. *Adv Energ Mater*, 2017, 7: 1601066–1601077
41 Sathiya M, Ramesha K, Rousse G, Foix D, Gonbeau D, Prakash AS, Doublet ML, Hemalatha K, Tarascon JM. *Chem Mater*, 2013, 25: 1121–1131
42 Thackeray MM, Kang SH, Johnson CS, Vaughey JT, Benedek R, Hackney SA. *J Mater Chem*, 2007, 17: 3112–3125
43 Yabuuchi N, Yoshii K, Myung ST, Nakai I, Komaba S. *J Am Chem Soc*, 2011, 133: 4404–4419
44 Yu H, Zhou H. *J Phys Chem Lett*, 2013, 4: 1268–1280
45 Johnson CS, Li N, Lefief C, Vaughey JT, Thackeray MM. *Chem Mater*, 2008, 20: 6095–6106
46 Yu H, So YG, Kuwabara A, Tochigi E, Shibata N, Kudo T, Zhou H, Ikuhara Y. *Nano Lett*, 2016, 16: 2907–2915
47 Xu Y, Hu E, Yang F, Corbett J, Sun Z, Lyu Y, Yu X, Liu Y, Yang XQ, Li H. *Nano Energy*, 2016, 28: 164–171
48 Hu E, Lyu Y, Xin HL, Liu J, Han L, Bak SM, Bai J, Yu X, Li H, Yang XQ. *Nano Lett*, 2016, 16: 5999–6007
49 Zhao E, Liu X, Hu Z, Sun L, Xiao X. *J Power Sources*, 2015, 294: 141–149
50 Jarvis KA, Deng Z, Allard LF, Manthiram A, Ferreira PJ. *Chem Mater*, 2011, 23: 3614–3621
51 Sathiya M, Rousse G, Ramesha K, Laisa CP, Vezin H, Sougrati MT, Doublet ML, Foix D, Gonbeau D, Walker W, Prakash AS, Ben Hassine M, Dupont L, Tarascon JM. *Nat Mater*, 2013, 12: 827–835
52 Miura Y, Yasui Y, Sato M, Igawa N, Kakurai K. *J Phys Soc Jpn*, 2007, 76: 033705
53 Salager E, Sarou-Kanian V, Sathiya M, Tang M, Leriche JB, Melin P, Wang Z, Vezin H, Bessada C, Deschamps M, Tarascon JM. *Chem Mater*, 2014, 26: 7009–7019
54 Sathiya M, Abakumov AM, Foix D, Rousse G, Ramesha K, Saubanère M, Doublet ML, Vezin H, Laisa CP, Prakash AS, Gonbeau D, VanTendeloo G, Tarascon JM. *Nat Mater*, 2015, 14: 230–238
55 Lee J, Urban A, Li X, Su D, Hautier G, Ceder G. *Science*, 2014, 343: 519–522
56 Lee J, Seo DH, Balasubramanian M, Twu N, Li X, Ceder G. *Energy Environ Sci*, 2015, 8: 3255–3265
57 Yabuuchi N, Takeuchi M, Nakayama M, Shiiba H, Ogawa M, Nakayama K, Ohta T, Endo D, Ozaki T, Inamasu T, Sato K, Komaba S. *Proc Natl Acad Sci USA*, 2015, 112: 7650–7655
58 Glazier SL, Li J, Zhou J, Bond T, Dahn JR. *Chem Mater*, 2015, 27: 7751–7756
59 Wang R, Li X, Liu L, Lee J, Seo DH, Bo SH, Urban A, Ceder G. *ElectroChem Commun*, 2015, 60: 70–73
60 Pralong V, Gopal V, Caignaert V, Duffort V, Raveau B. *Chem Mater*, 2012, 24: 12–14
61 Qing RP, Shi JL, Zhai YB, Zhang XD, Yin YX, Gu L, Guo YG. *ElectroChim Acta*, 2016, 196: 749–755
62 Zheng J, Xu P, Gu M, Xiao J, Browning ND, Yan P, Wang C, Zhang JG. *Chem Mater*, 2015, 27: 1381–1390
63 Luo K, Roberts MR, Hao R, Guerrini N, Pickup DM, Liu YS, Edström K, Guo J, Chadwick AV, Duda LC, Bruce PG. *Nat Chem*, 2016, 8: 684–691
64 Qiu B, Zhang M, Xia Y, Liu Z, Meng YS. *Chem Mater*, 2017, 29: 908–915
65 Kang K, Meng YS, Bréger J, Grey CP, Ceder G. *Science*, 2006, 311: 977–980
66 Zhao E, Chen M, Chen D, Xiao X, Hu Z. *ACS Appl Mater Interfaces*, 2015, 7: 27096–27105
67 Lu Z, Beaulieu LY, Donaberger RA, Thomas CL, Dahn JR. *J Electrochem Soc*, 2002, 149: A778
68 Lu Z, Dahn JR. *J Electrochem Soc*, 2002, 149: A815
69 Koga H, Croguennec L, Ménétrier M, Mannessiez P, Weill F, Delmas C. *J Power Sources*, 2013, 236: 250–258
70 Koga H, Croguennec L, Menetrier M, Douhil K, Belin S, Bourgeois L, Suard E, Weill F, Delmas C. *J ElectroChem Soc*, 2013, 160: A786–A792
71 Armstrong AR, Holzapfel M, Novak P, Johnson Christopher S, Kang Sun-Ho, Thackeray Michael M, Bruce Peter G. *J Am Chem Soc*, 2006, 128: 8694–8698
72 Hy S, Felix F, Rick J, Su WN, Hwang BJ. *J Am Chem Soc*, 2014, 136: 999–1007
73 Seo DH, Lee J, Urban A, Malik R, Kang SY, Ceder G. *Nat Chem*, 2016, 8: 692–697
74 Goodenough JB, Park KS. *J Am Chem Soc*, 2013, 135: 1167–1176
75 Zhao E, Chen M, Hu Z, Xiao X, Chen D. *ElectroChim Acta*, 2016, 208: 64–70
76 Yu X, Lyu Y, Gu L, Wu H, Bak SM, Zhou Y, Amine K, Ehrlich SN, Li H, Nam KW, Yang XQ. *Adv Energ Mater*, 2014, 4: 1300950–1300960